X-RAYS FROM MARS

KONRAD DENNERL
Max-Planck-Institut für extraterrestrische Physik, Giessenbachstraße, 85748 Garching, Germany
(E-mail: kod@mpe.mpg.de)

(Received 23 February 2006; Accepted in final form 16 August 2006)

Abstract. X-rays from Mars were first detected in July 2001 with the satellite Chandra. The main source of this radiation was fluorescent scattering of solar X-rays in its upper atmosphere. In addition, the presence of an extended X-ray halo was indicated, probably resulting from charge exchange interactions between highly charged heavy ions in the solar wind and neutrals in the Martian exosphere. The statistical significance of the X-ray halo, however, was very low. In November 2003, Mars was observed again in X-rays, this time with the satellite XMM-Newton. This observation, characterized by a considerably higher sensitivity, confirmed the presence of the X-ray halo and proved that charge exchange is indeed the origin of the emission. This was the first definite detection of charge exchange induced X-ray emission from the exosphere of another planet. Previously, this kind of emission had been detected from comets (which are largely exospheres) and from the terrestrial exosphere. Because charge exchange interactions between atmospheric constituents and solar wind ions are considered as an important nonthermal escape mechanism, probably responsible for a significant loss of the Martian atmosphere, X-ray observations may lead to a better understanding of the present state of the Martian atmosphere and its evolution. X-ray images of the Martian exosphere in specific emission lines exhibited a highly anisotropic morphology, varying with individual ions and ionization states. With its capability to trace the X-ray emission out to at least 8 Mars radii, XMM-Newton can explore exospheric regions far beyond those that have been observationally explored to date. Thus, X-ray observations provide a novel method for studying processes in the Martian exosphere on a global scale.

Keywords: Mars, X-rays, solar wind, charge exchange, X-ray scattering

1. Introduction

Since July 2001 we have known that Mars is an X-ray source. Mars is the fourth planet found to emit X-rays, after the Earth (e.g. Winckler *et al*., 1958; Grader *et al*., 1968), Jupiter (Metzger *et al*., 1983) and Venus (Dennerl *et al*., 2002). The first X-ray observations of Mars were made with the ROSAT satellite (Trümper, 1983) on three occasions during April 10–13, 1993, yielding a total exposure of 75 minutes. However, during two observations, Mars was unfavourably placed in the field of view of the ROSAT Position Sensitive Proportional Counter (Pfeffermann *et al*., 1986), so that only 35 minutes of exposure were left to search for any X-ray emission, and no X-ray signal was detected (Dennerl, 2002).

The motivation for the ROSAT observation was to reveal the relative significance of Thomson scattering, fluorescent scattering and airglow in Mars'

Space Science Reviews (2006) 126: 403–433
DOI: 10.1007/s11214-006-9028-7

predominantly CO_2 atmosphere. In 1996, the discovery of comets as a new, unexpected class of bright X-ray sources (Lisse *et al*., 1996; Dennerl *et al*., 1997; Mumma *et al*., 1997) led to an increased interest in X-ray studies of solar system objects. It revealed the importance of another process for the generation of soft X-rays which was overlooked for a long time: charge exchange between highly charged heavy ions in the solar wind and neutral gas in the solar system (Cravens, 1997).

Mars has a tenuous atmosphere, a weak magnetic field, and orbits at a heliocentric distance where comets exhibit significant activity. Mars can thus be considered as a planetary analog to a comet, and it is reasonable to expect that the same solar wind charge exchange processes which cause comets to emit X-rays also operate in the Martian exosphere. This possibility was investigated by Cravens (2000) and Krasnopolsky (2000). Holmström *et al*. (2001) made predictions about the X-ray morphology based on detailed computer simulations. The other likely source of X-ray radiation from Mars was scattering of solar X-rays, which was studied by Cravens and Maurellis (2001). All these model investigations were prior to the detection of X-rays from Mars.

2. First Detection of X-rays from Mars

On 4 July 2001, X-rays from Mars were detected for the first time (Dennerl, 2002). The observation was performed with the ACIS-I detector on the Chandra X-ray satellite. With its unprecedentedly high spatial resolution, Chandra was excellently suited for an observation of Mars. Furthermore, in contrast to other X-ray satellites which can observe only at directions which are approximately perpendicular to the direction of the Sun, Chandra was the first imaging X-ray satellite which was able to observe Mars around opposition, when it is closest to Earth.

Although the closest approach of Mars to Earth, with a minimum distance of 0.45 AU, had occurred already on 22 June 2001, the Chandra observation was postponed by two weeks. This decision was motivated by the fact that Mars was expected to be an X-ray source mainly due to fluorescent scattering of solar X-rays, and computer simulations of this process, already successfully tested on Venus (Dennerl *et al*., 2002), had indicated that observing at a non-zero phase angle would result in a diagnostically more valuable image than observing at opposition: while a practically uniform X-ray brightness across the whole planet was expected for a phase angle close to zero, a phase angle of $\sim 15^\circ$ should already result in a characteristic X-ray brightening on the sunward limb. The decision to postpone the Chandra observation was also supported by the favorable fact that Mars was still approaching the perihelion of its orbit, so that its distance from the Earth would increase only slightly. Furthermore, the small loss of X-ray photons due to the

reduced solid angle would be almost compensated by the fact that Mars would then be closer to the Sun and would intercept more solar radiation.

At the time of the observation, Mars was at a heliocentric distance of 1.45 AU and at a geocentric distance of 0.46 AU. Its diameter was 20.3″, and it was observed at a phase angle of 18.2° and at a solar elongation of 153.7°. The Chandra observation lasted for 9 hours and 13 minutes. During this time, the satellite did not track Mars, but kept its orientation fixed with respect to the sky. As seen from the orbit of Chandra, Mars was moving along a curved path across the sky, and this path was directly visible in the X-ray image (Figure 1). The photons were detected with X-ray CCDs which were read out every 3.2 s, so that a post-facto transformation of the individual photons into the rest frame of Mars was possible, resulting in the first X-ray image of this planet (Figure 2).

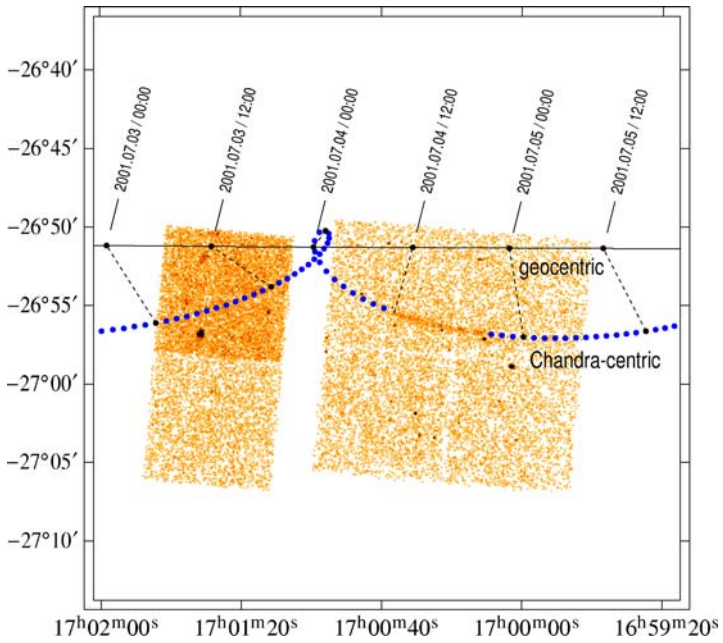

Figure 1. Apparent motion of Mars in celestial coordinates (J 2000), as seen from the Earth and Chandra. The solid line shows the geocentric path of Mars, with its position indicated every 12 hours. Dashed lines illustrate the parallactic shift at these times due to the Chandra orbit. Chandra-centric positions are shown every hour by dots, which match the apparent size of Mars. The loop at 4 July, 0 UT reflects the perigee passage of Chandra. Superimposed on this diagram is the Chandra image in celestial coordinates, obtained at $E < 1.0$ keV. The sequence of dots in the Chandra-centric curve is interrupted to show the curved soft X-ray trail of Mars on the X-ray CCDs. In addition to Mars, several point sources show up in the Chandra image. The photons from these sources were excluded in the subsequent analysis (from Dennerl, 2002).

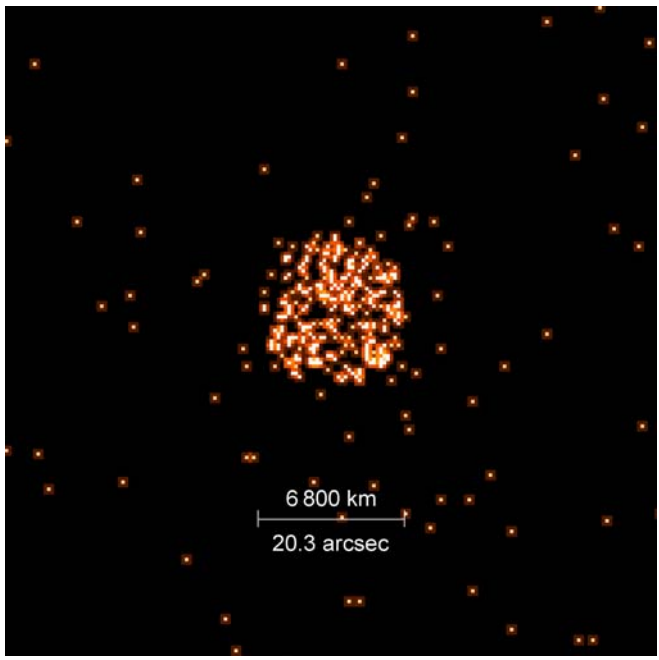

Figure 2. First X-ray image of Mars, obtained with Chandra ACIS-I on 4 July 2001. Only photons in the instrumental energy range $E = 0.40$–0.73 keV were selected and transformed into the rest frame of Mars. Trails of point sources were removed (from Dennerl, 2002).

3. Scattering of Solar X-rays

Mars appeared as an almost fully illuminated disk, with an indication of the phase effect predicted by the earlier computer simulations of the scattering of solar X-rays in its atmosphere. These simulations concentrated on fluorescent scattering, because this process was expected to be the dominant one. Cravens and Maurellis (2001) found that the X-ray intensity due to fluorescence of O and N alone exceeds that of elastic scattering in the broad spectral band 2–120 Å (0.1–6.2 keV) by a factor of 2.4.

In order to make a direct comparison of the observed X-ray image with that expected for fluorescent scattering of solar X-rays, these simulations were specifically tuned to the conditions of the Chandra observation (Dennerl, 2002). The ingredients to the simulation were the composition and density structure of the Martian atmosphere, the photoabsorption cross sections and fluorescence efficiencies of the major atmospheric constituents, and the incident solar spectrum.

Our knowledge about the Martian atmosphere is mainly based on spacecraft observations, in particular the Viking 1 and 2 missions (e.g. Nier and McElroy, 1977). More recently, the Mars Global Surveyor and Mars Odyssey accelerometer

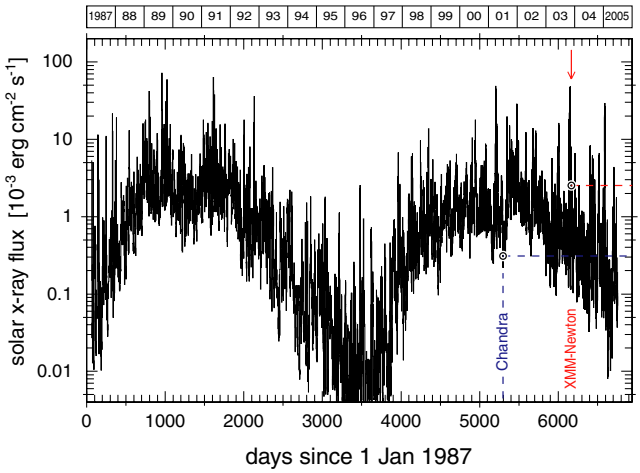

Figure 3. 1–8 Å (1.55–12.4 keV) solar X-ray flux at 1.0 AU, measured with the GOES satellites. The times of the Chandra and XMM-Newton observations are marked, together with the corresponding mean solar X-ray flux, which was highly variable during the XMM-Newton observation (from Dennerl *et al.*, 2006a).

measurements, obtained during aerobraking, revealed the large-scale and small-scale structure of the thermosphere in unprecedented detail (Withers, 2006). With this information, sophisticated models are being developed, like the Mars Global Reference Atmospheric Model (Mars-GRAM), an engineering-level Mars atmosphere model which is widely used for many Mars mission applications (e.g. Justus *et al.*, 2005).

For the purpose of modeling the scattering of solar X-rays in the Martian atmosphere, a simplified model was adopted, which describes the total density in the form of analytical expressions for different phases of the solar cycle (Sehnal, 1990a,b). This model is based on the COSPAR Reference Atmosphere of Mars together with Viking 1 and 2 measurements and theoretical considerations. Motivated by the general behaviour of the soft solar X-ray flux (Figure 3), solar maximum conditions were selected (Figure 4[1]). For simplicity it was assumed that the Martian atmosphere is composed of C, N, and O only, neglecting the ∼1.6% contribution of other elements, mainly Ar, and the following composition was used: 64.9% oxygen, 32.4% carbon, and 2.7% nitrogen. As the main constituents, C and O, are contained in CO_2, this composition was assumed to be homogeneous throughout the atmosphere. Viking 1 and 2 measurements showed that the Martian atmosphere is mixed to heights in excess of 120 km (Nier and McElroy, 1977). Above the homopause,

[1] In Dennerl (2002), a definition was adopted where the exosphere starts at 100 km, while 180–250 km is a more realistic value; for practically all planetary exospheres, the exobase occurs near a density of $\sim 10^8$ cm^{-3}. The 100–180 km region is generally defined as the thermosphere. The labels in Figures 4, 6, and 7 have been changed accordingly.

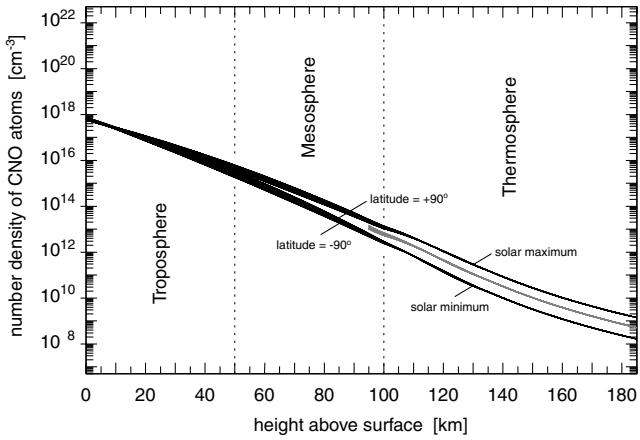

Figure 4. Number density $n_{\mathrm{CNO}} = n_{\mathrm{C}} + n_{\mathrm{N}} + n_{\mathrm{O}}$ of the sum of C, N, and O atoms in the Mars model atmosphere (Sehnal, 1990a,b) as a function of the height above the surface, for solar minimum, solar maximum, and the intermediate state. Below 100 km, the density depends also on the latitude (adapted from Dennerl, 2002).

at $\sim$110 km, different species start separating out according to their mass: first O, then H_2 and H take over as the most abundant species.

From the photoabsorption cross sections (e.g. Reilman and Manson, 1979) and the C, N, and O contributions listed above, the effective cross section of the Martian atmosphere was computed (Figure 5a). This, together with the atmospheric density structure, yielded its optical depth, as seen from outside (Figure 6). It turned out that, at solar maximum, the Martian atmosphere becomes optically thick to photoabsorption of incident solar X-rays with $E = 0.1$–1.0 keV between 113 km and 100 km. The solar spectrum for the time of the Chandra observation was derived from SOLAR 2000 (Tobiska *et al*., 2000). To improve the coverage towards energies above 100 eV, synthetic spectra were computed with the model of Mewe *et al*. (1985) and aligned with the SOLAR 2000 spectrum by adjusting the temperature and intensity. The resulting spectrum, scaled to the heliocentric distance of Mars, is shown in Figure 5b (upper curve).

For the simulation, the irradiated part of the Martian atmosphere was sampled with a grid of cubic volume elements with a side length of 1 km. Following the direction of the incoming solar X-rays, the absorbed radiation was then computed for each volume element. Figure 5b (lower curve) illustrates how the incident solar spectrum is modified by atmospheric photoabsorption. Only a small part of the absorbed energy, however, is emitted in the form of fluorescent photons, because of the small fluorescent yields for C, N, O (0.25%, 0.55%, and 0.85%, respectively; Krause, 1979). Figure 7 shows the resulting volume emissivities of fluorescence photons for the subsolar atmospheric column (zenith angle 0°) and for a column at the terminator (zenith angle 90°). The height of maximum emissivity rises with

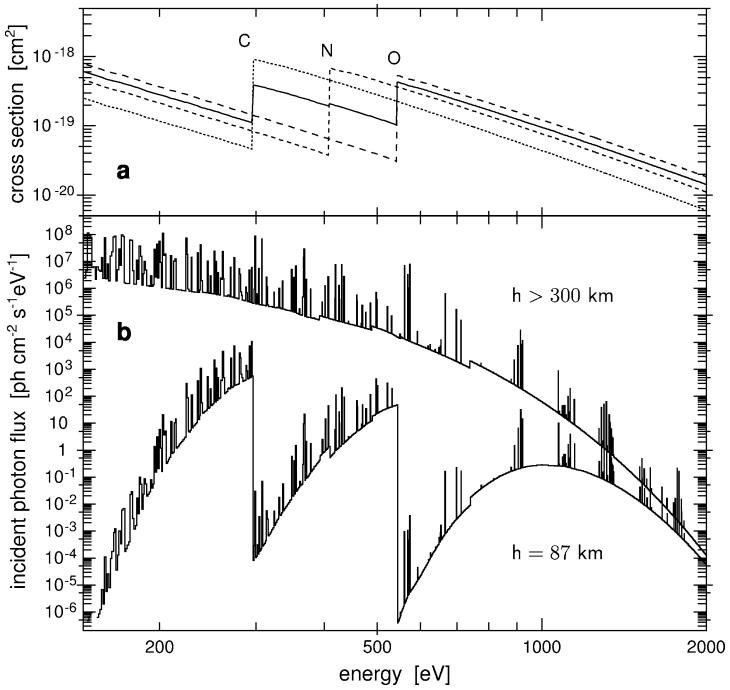

Figure 5. (a) Photoabsorption cross sections σ_C, σ_N, σ_O for C, N, and O (dashed lines), and σ_{CNO} for the chemical composition of the Mars atmosphere (solid line). (b) Incident solar X-ray photon flux on top of the Mars atmosphere ($h > 300$ km) and at 87 km height. The spectrum is plotted in 1 eV bins. At 87 km, it is considerably attenuated just above the K_α absorption edges, recovering towards higher energies (from Dennerl, 2002).

increasing solar zenith angle because of the increased path length and absorption along oblique solar incidence angles. By sampling the radiation in the volume elements along the line of sight, starting from the element which is farthest away from the observer, synthetic X-ray images of Mars were then accumulated in the fluorescence energies of C, N, O for the phase angle of the Chandra observation.

These images (Figure 8a–c) exhibited a fairly uniform glow of the disk accomanied by a pronounced limb brightening on the sunward side. This is due to the fact that the scattering of solar X-rays is most efficient in the upper atmospheric regions, at heights above ∼100 km, and extends into the tenuous, optically thin parts of the thermosphere (Figure 7). There, the volume emissivities add up along the line of sight without considerable absorption, so that the observed brightness is mainly determined by the extent of the atmospheric column along the line of sight. As a result, the sun-lit hemisphere of Mars appears surrounded by an almost transparent luminous shell in X-rays, and Mars looks brightest at the sunward limb since more luminous material is there.

Detailed comparison of the simulated images (Figure 8a–c) shows that the amount of limb brightening is somewhat different for the three energies. According

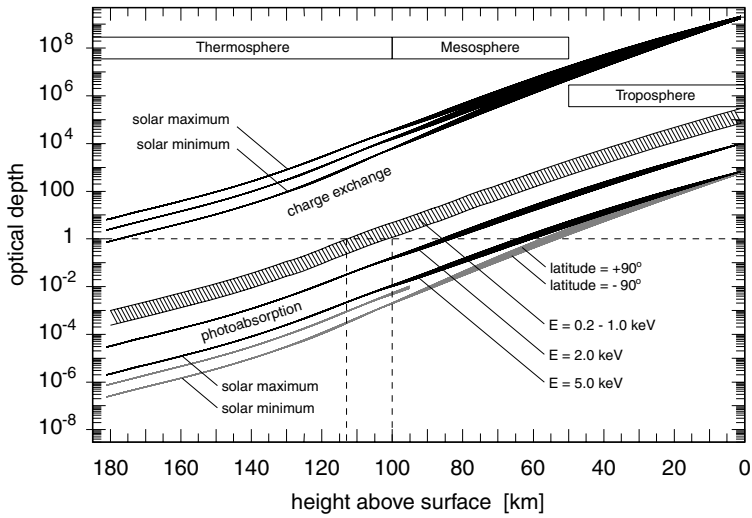

Figure 6. Optical depth $\tau = \tau_C + \tau_N + \tau_O$ of the Martian model atmosphere (Sehnal, 1990a,b) with respect to charge exchange (above) and photoabsorption (below), as seen from outside. The upper/lower boundaries of the hatched area refer to energies just above/below the C and O edges (cf. Figure 5a). For better clarity the dependence of the photoabsorption on the solar cycle is only shown for $E = 5.0$ keV; the curves for the other energies refer to the solar maximum. The dashed horizontal line, at $\tau = 1$, marks the transition between the transparent ($\tau < 1$) and opaque ($\tau > 1$) region. For charge exchange interactions, a constant cross section of $3 \cdot 10^{-15}$ cm^2 was assumed. Due to this high cross section, $\tau = 1$ is reached already at heights of 180 km and above; even for exospheric hydrogen, the opacity to charge exchange is of the order of 0.1 and not negligible. For photoabsorption at $E = 0.2$–1.0 keV, the atmosphere becomes opaque between 113 km and 100 km for solar maximum conditions. During solar minimum, this transition occurs ~10 km deeper in the atmosphere (adapted from Dennerl, 2002).

to the computer simulations, this brightening depends sensitively on the density and chemical composition of the Martian atmosphere. Thus, precise measurements of this brightening could provide a novel method of obtaining remotely direct information about the atmospheric structure in the mesosphere and thermosphere, for different phases of the solar cycle. A direct comparison of the simulated images with the Chandra image (Figure 8d), however, suffers from low photon statistics, as only ~300 photons were detected from Mars during the whole observation. Nevertheless, the predicted limb brightening can be seen in the surface profiles (Figure 11b), which show also indications for a fading on the opposite side, in agreement with the simulation.

Mars is an extremely faint X-ray source: its observed X-ray flux was only 5×10^{-10} of the optical flux. Taking into account that the energy of an X-ray photon exceeds that of an optical photon by two orders of magnitude, this means that there was on average only one X-ray photon among 2×10^{11} photons from Mars. This extremely low number of X-ray photons in the Mars spectrum is due

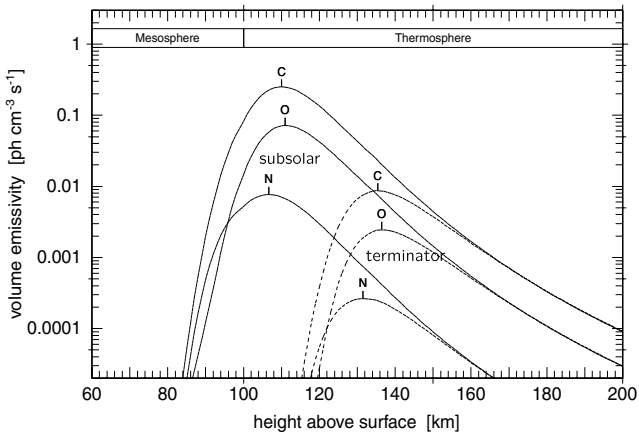

Figure 7. Volume emissivities of C, N, and O K_α fluorescent photons at zenith angles of 0° (subsolar, solid lines) and 90° (terminator, dashed lines) for the incident solar spectrum of Figure 5b. In all cases the maximum emissivity occurs in the thermosphere, where the optical depth depends also on the solar cycle (Figure 6; adapted from Dennerl, 2002).

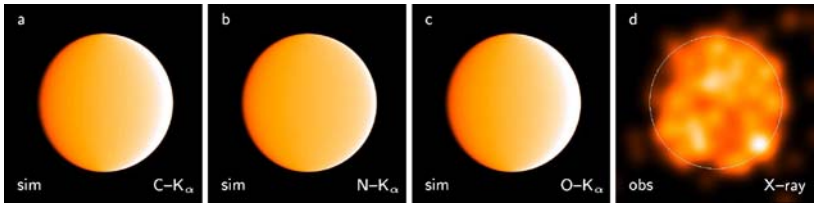

Figure 8. (a–c) Simulated X-ray images of Mars at C-K_α, N-K_α, and O-K_α, for the phase angle of the Chandra observation (18.2°). All images show some limb brightening, especially at C-K_α and O-K_α. (d) Observed X-ray image, accumulated in the energy range 0.4–0.7 keV and smoothed with a Gaussian function with $\sigma = 1.2''$. The circle indicates the geometric size of Mars. This image is dominated by O-K_α fluorescence photons. Although the brightness fluctuations are mainly caused by photon statistics and are not significant, there is evidence for limb brightening on the right-hand (sunward) side (cf. Figure 11b; from Dennerl, 2002).

to the low X-ray flux of the Sun and the low X-ray albedo of the Martian CO_2 atmosphere, which is in turn caused by the very low X-ray fluorescence yields of light elements.

In order to calculate the X-ray luminosity, it is necessary to know the angular distribution of the scattered solar X-rays, as these photons are not emitted isotropically. For this purpose, X-ray intensities were determined from synthetic images for different phase angles (Figure 9). By spherically integrating these intensities for the three fluorescence energies over phase angle, the following luminosities were obtained from the simulation: 2.9 MW for C, 0.1 MW for N, and 1.7 MW for O. These values, directly derived from the solar spectrum, the Mars model atmosphere and quantities from atomic physics, thus predicted a total X-ray luminosity of 4.7 MW.

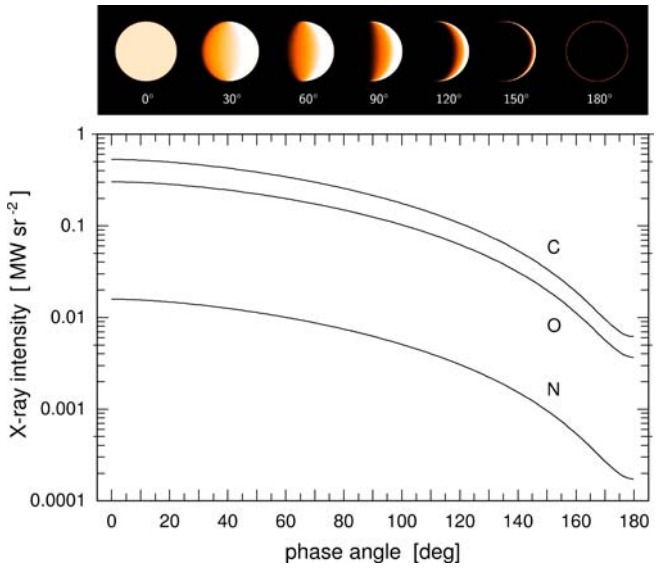

Figure 9. X-ray intensity of Mars as a function of phase angle, in the fluorescence lines of C, N, and O, for the conditions of 4 July 2001. The images at top, all displayed in the same intensity coding, illustrate the appearence of Mars at O-K$_\alpha$ for selected phase angles. Depending on the incident solar spectrum, there may be episodes when the O-K$_\alpha$ flux exceeds that of C-K$_\alpha$ (from Dennerl, 2002).

The corresponding value, obtained from the observed flux, was $\sim 3.5 \pm 0.6$ MW. Both values agreed well with the prediction of Cravens and Maurellis (2001), who had estimated a luminosity of 2.5 MW due to X-ray fluorescence, with an uncertainty factor of about two.

The first X-ray spectrum of Mars (Figure 10), obtained with the ACIS-I detector onboard Chandra, was dominated by a single narrow emission line. Although this line appeared at 0.65 keV, it was interpreted as the O-K$_\alpha$ fluorescence line at 0.53 keV. This conclusion was motivated by the fact that in the case of Venus a similar line, observed at 0.6 keV with the same detector, could be uniquely identified to be at 0.53 keV by an additional observation with an X-ray grating (LETG; Dennerl *et al*., 2002). The apparent energy shift was most likely caused by optical loading, a superposition of the charges released by 0.53 keV photons and optical photons, during the 3.2 s exposure of each CCD frame. The other expected emission lines, from C and N fluorescence, were too close or even outside the sensitivity range of the ACIS-I detector. Thus, the observed X-ray morphology, the luminosity, and the X-ray spectrum were all in full agreement with fluorescent scattering of solar X-rays.

No evidence for temporal variability was found. This was also in agreement with fluorescent scattering of solar X-rays, because the solar X-ray flux was quite steady at that time. Dennerl (2002) noticed that the conditions encountered during

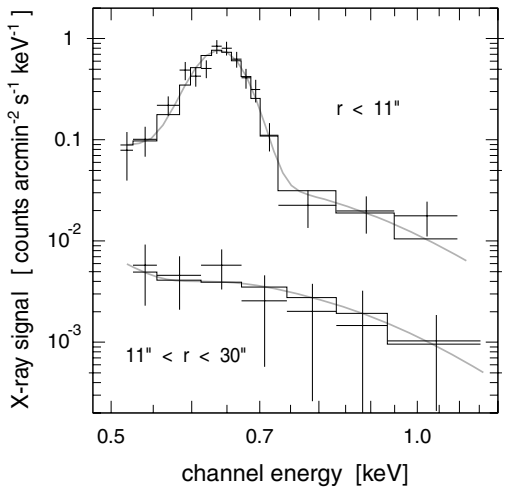

Figure 10. X-ray spectra (background subtracted) of the Martian disk (top) and halo (bottom), obtained with Chandra ACIS-I. The disk spectrum is dominated by a single narrow emission line, caused by O-K$_\alpha$ fluorescence and shifted to higher energies due to optical loading. At higher energies the presence of an additional component is indicated. The spectral shape of this component agrees with that of the halo (from Dennerl, 2002).

this observation were favorable for testing the hypothesis of dust-related X-ray emission: scattering of solar X-rays on very small dust particles was one of the early suggestions for explaining the X-ray emission from comets. Wickramasinghe and Hoyle (1996) had noted that X-rays could be efficiently scattered by dust particles, if their size is comparable to the X-ray wavelength. Such attogram dust particles ($\sim 10^{18}$ g) would be difficult to detect by other means. Their existence was postulated by Owens *et al*. (1998) in order to explain the X-ray properties of comet C/1995 O1 (Hale-Bopp). There was the possibility that such particles might be present in the upper Mars atmosphere, in particular during episodes of global dust storms.

Incidentally, on June 24 a local dust storm on Mars had originated and expanded quickly, developing into a planet-encircling dust storm by July 11. Such dust storms have been observed on roughly one-third of the perihelion passages during the last decades, but never so early in the Martian year. On July 4, this very vigorous storm had covered roughly one hemisphere – the hemisphere that happened to be visible at the beginning of the Chandra observation. By the end of the observation, which lasted for one third of a Mars rotation, this hemisphere had mainly rotated away from our view. Thus, a comparison of the Chandra data from both regions would have revealed any influence of the dust storm on the X-ray flux.

There was, however, no change in the mean X-ray flux between the first and second half of the observation, where 150 and 157 photons were detected, respectively

(Dennerl, 2002). This implied that, if attodust particles were present in the upper Mars atmosphere, the dust storm did not lead to a local increase in their density, high enough to modify the observed X-ray flux significantly. No statement, however, could be made about the situation below ∼80 km, as the solar X-rays do not reach these atmospheric layers. While the presence of some attodust in the upper atmosphere could not be ruled out by the Chandra observation, the fact that the X-ray spectrum of Mars was dominated by a single emission line showed that any contribution of such particles to the X-ray flux from Mars must be small compared to fluorescence, even in the process of a developing global dust storm.

While all the properties of the observed X-ray radiation from Mars were fully consistent with fluorescent scattering of solar X-rays in the upper atmosphere as the dominant source, there were, however, also indications for the presence of an additional component of a completely different origin. This will be discussed in the next section.

4. Charge Exchange Induced X-ray Emission

An exciting feature in Figure 11b is the gradual decrease of the X-ray surface brightness between 1 and ∼3 Mars radii, indicating the presence of a soft X-ray halo around Mars. Although the excess of X-ray photons in this region was only $\sim 35 \pm 8$ relative to the background expected for this area, the spectral distribution of these photons was different from those of Mars and the sky background. This ruled out the possibility that the halo was caused by, e.g., the optics of the X-ray telescope. Furthermore, the presence of a component with the same spectral distribution as in the halo was indicated in the spectrum of the Mars disk. Within the very limited statistical quality, the spectrum of the halo resembled that of comets, in particular those which had been discovered in archival ROSAT data (Dennerl *et al.*, 1997). In analogy to the situation at comets, Dennerl (2002) interpreted these findings as evidence for the presence of an X-ray halo around Mars caused by charge exchange interactions between highly charged heavy ions in the solar wind and neutrals in the Martian exosphere (SWCX).

Among the protons, electrons and alpha particles, the solar wind also contains a small fraction, about 0.1%, of heavier particles in highly charged states, such as C^{6+}, N^{6+}, O^{6+}, Ne^{8+}, Si^{9+}, Fe^{11+}. They obtain this high degree of ionization in the hot solar corona, which has a temperature of several million degrees, before they leave the Sun at some hundred kilometers per second. On their trip through the solar system in the tenuous solar wind, these ions usually have no chance to capture the missing electrons. They remain in the highly ionized state until they hit sufficiently dense matter, e.g. a comet, where electrons are available in large numbers, mostly bound in H_2O molecules. When solar wind ions capture

such electrons, they attain highly excited states and radiate a large fraction of the excitation energy in the extreme ultraviolet and X-ray range. The ionized molecule or atom may subsequently capture a free electron from the solar wind and return to its neutral state.

Triggered by the discovery of cometary X-ray emission (Lisse *et al*., 1996; Dennerl *et al*., 1997; Mumma *et al*., 1997) and the subsequent finding that this emission is caused by SWCX (Cravens, 1997), the consequences of this process for the X-ray emission of Mars had already been investigated by several authors. Cravens (2000) predicted an X-ray luminosity of ∼0.01 MW. Krasnopolsky (2000) estimated an X-ray emission of $\sim 4 \cdot 10^{22}$ ph s^{-1}. Adopting an average photon energy of 200 eV (e.g. Cravens, 1997), this corresponds to an X-ray luminosity of 1.3 MW. Holmström *et al*. (2001) computed a total X-ray luminosity of Mars due to charge exchange (within 10 Mars radii) of 1.5 MW at solar maximum, and 2.4 MW at solar minimum.

For the X-ray halo observed within 3 Mars radii, excluding Mars itself, the Chandra observation yielded a flux of $(0.9 \pm 0.4) \cdot 10^{-14}$ erg cm^{-2} s^{-1} in the energy range $E = 0.5$–1.2 keV (Dennerl, 2002). Assuming isotropic emission, this flux corresponds to a luminosity of 0.5 ± 0.2 MW. Taking all the uncertainties into account, this value agrees well with the predictions of Krasnopolsky (2000) and Holmström *et al*. (2001), in particular when the spectral shape is extrapolated to lower energies. Using the abundances of H, H_2, and hot oxygen in the Martian exosphere, Krasnopolsky and Gladstone (2005) compared the observed X-ray luminosity of the Martian X-ray halo with that expected for solar wind charge exchange, and obtained consistent results.

The estimates above indicate that the SWCX process is indeed able to produce the observed number of X-ray photons. In order to answer the question whether also their spatial distribution (Figure 11b) can be reproduced, simulations are necessary. Holmström *et al*. (2001) presented results of such simulations already prior to the Chandra observation of Mars. They used an empirical, axial symmetric model of the proton flow for computing the ion velocities and densities. Under the assumption that the magnetic field is frozen into the flow, they derived from the velocity model the global electric and magnetic fields, which enabled them to study the acceleration of the ions by the Lorentz force near Mars. This allowed them to calculate trajectories of heavy solar wind ions (e.g. Figure 13a), their charge exchange interactions with neutrals in the Martian exosphere, and the resulting X-ray emission.

The simulated SWCX images of Mars, reproduced in Figure 13b for different phase angles, show a dark Mars embedded in an extended, diffuse X-ray halo. This morphology is completely different from that of X-ray fluorescence (cf. Figures 8a–c, 9). The simulated SWCX images for a phase angle of 0° and 30° (top row in Figure 13b) show a good qualitative agreement with the observed X-ray brightness profiles (Figure 11b), even in the detail that the halo is brighter at the "dayside" than at the "nightside". The simulated SWCX images were computed by Holmström

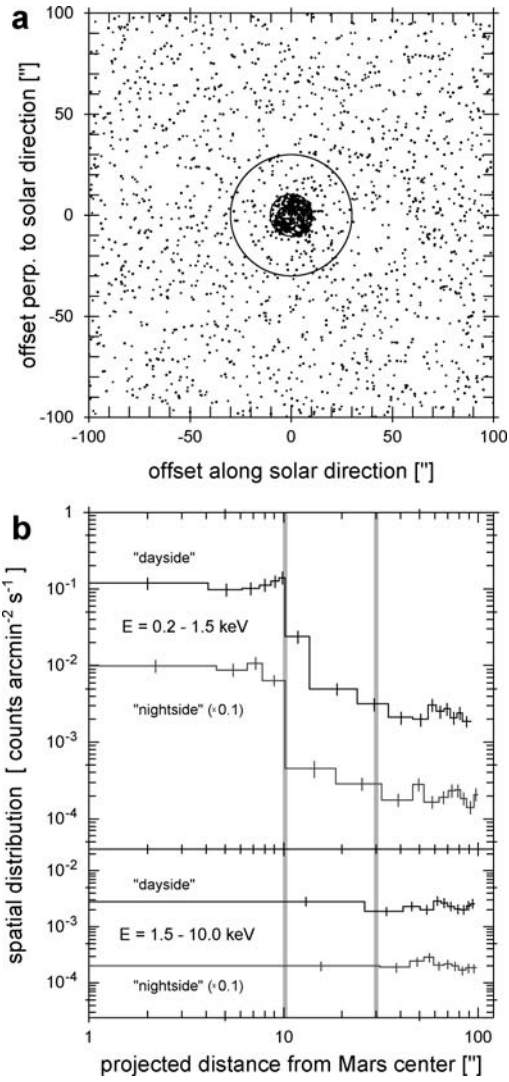

Figure 11. Radial distribution of photons around Mars in the Chandra observation. (a) All photons in the energy range 0.2–10.0 keV. The inner circle, with $r = 10.2''$, shows the geometric size of Mars, while the outer one, at $r = 30''$, illustrates the extent of the soft X-ray halo. (b) Spatial distribution of the photons in the soft ($E = 0.2$–1.5 keV) and hard ($E = 1.5$–10.0 keV) energy range, separately for the "dayside" (offset along projected solar direction > 0) and the "nightside" (offset < 0); note, however, that the phase angle was only 18.2°. For better clarity the nightside histograms were shifted by one decade downward. The thick vertical lines mark the radii $10.2''$ and $30''$ of the circles in (a) (from Dennerl, 2002).

et al. (2001) for average solar wind conditions at solar minimum. As these conditions and the phase angle were different during the Chandra observation, only qualitative agreement can be expected.

In order to make a direct comparison with the Chandra results, Gunell *et al*. (2004) computed the expected X-ray emission from Mars due to SWCX for the specific conditions of the Chandra observation. The solar wind parameters were estimated from data obtained by the WIND spacecraft two days before the X-ray observation. Since Mars was near opposition, plasma that was sampled by WIND near the Earth reached the Mars environment approximately two days later. The solar wind density was scaled with the square of the heliocentric distance ratio of Earth and Mars, and the direction of the magnetic field was assumed to follow a Parker spiral. The electric and magnetic fields around Mars were obtained by running a hybrid simulation of the interaction between the solar wind and Mars with 1.7×10^6 particles. Then, 10^9 trajectories of heavy solar wind ions in these electric and magnetic fields were calculated to get the corresponding SWCX induced X-ray emission, under the reasonable assumption of collisionally thin conditions. This calculation was done for the 15 ion species which were considered as the most important ones for SWCX induced X-ray emission.

The resulting X-ray image (Figure 12a) and radial surface brightness profile (Figure 12b) reproduced the overall shape of the observed X-ray photon distribution (Figure 11b) in the halo. Also the "dayside halo" was brighter than the "nightside halo", in agreement with the observation. However, a quantitative comparison revealed some differences: the calculated X-ray luminosity turned out to be higher than the observed one by a factor between one and three, and the simulated halo brightness dropped less steeply with radial distance than observed. Gunell *et al*. (2004) listed a number of uncertainties of the model that could cause deviations: the density of the neutral exosphere of Mars at the time of the observation, the solar wind parameters, the spatial resolution of the model, and uncertainties in the charge exchange cross sections.

The dependence of the simulation results on some of these parameters was investigated in a subsequent analysis by Gunell *et al*. (2005): the solar wind estimates derived from WIND data were compared with estimates resulting from MHD tomography based on interplanetary scintillation (IPS) data, and the influence of changes in the neutral exosphere was studied by varying the exobase temperature. This investigation was restricted to only two important ion species, O^{7+} and C^{6+}. It turned out that the IPS parameters produced a brighter and more compact X-ray image than the WIND parameters, with up to twice the surface brightness within 1.4 Mars radii, while the brightness distribution in the outer halo was similar for both parameter sets (Figure 14). Concerning the dependence on the exobase temperature, it was found that both the intensity and the extent of the X-ray emitting region increase with increasing exobase temperature (Figures 12c, 15). Another parameter influencing the properties of SWCX induced X-ray emission at Mars may be related to a specific property of the Martian crust: Holmström and Kallio

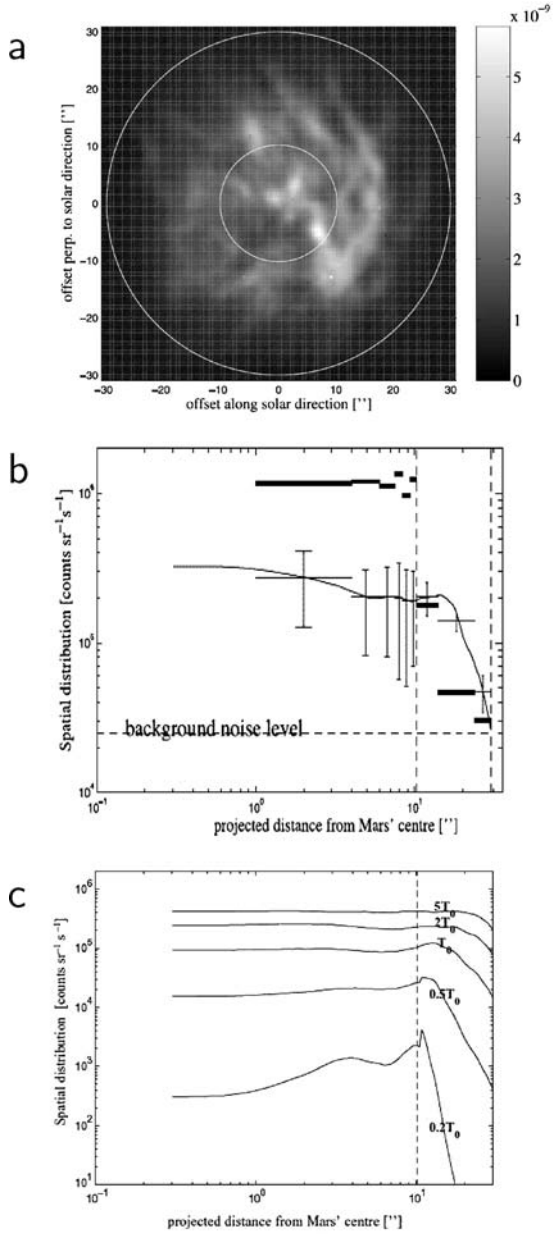

Figure 12. (a) Simulated X-ray image of Mars due to the SWCX process, computed for the conditions of the Chandra observation (Figure 11). (b) Corresponding radial distribution (thin solid curve) in comparison with the observed Chandra profile (thick horizontal lines). Note that the simulation does not take the flux contribution due to fluorescence into account (adapted from Gunell *et al.*, 2004). (c) Dependence of the radial distribution of simulated SWCX X-ray photons on the assumed exobase temperature (see Figure 15 for more information). From top to bottom, the nominal exobase temperatures have been scaled by a factor of 5; 2; 1; 0.5; and 0.2, respectively (from Gunell *et al.*, 2005).

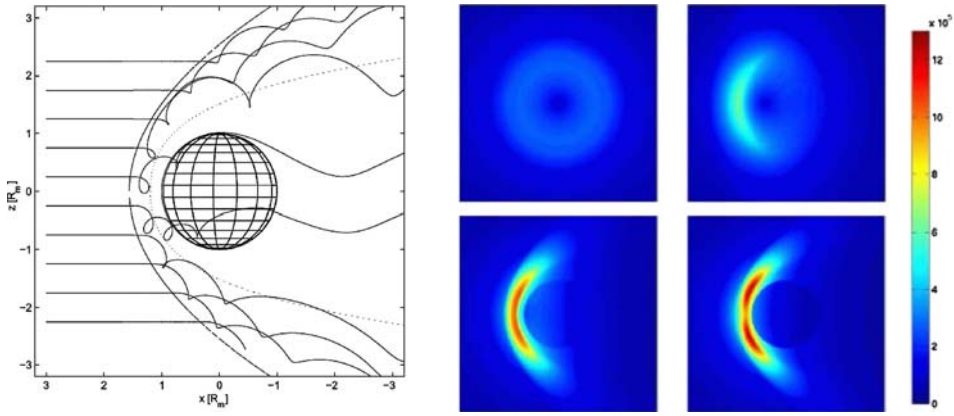

Figure 13. (a) Trajectories of solar wind O^{6+} ions around Mars for a magnetic field $B_{SW} = 4$ nT perpendicular to the image plane and for a velocity of 400 km s^{-1}. (b) Simulated images of the X-ray emission from Mars due to SWCX, for phase angles of 0° (top left), 30° (top right), 60° (bottom left) and 90° (bottom right), at solar minimum (from Holmström *et al.*, 2001).

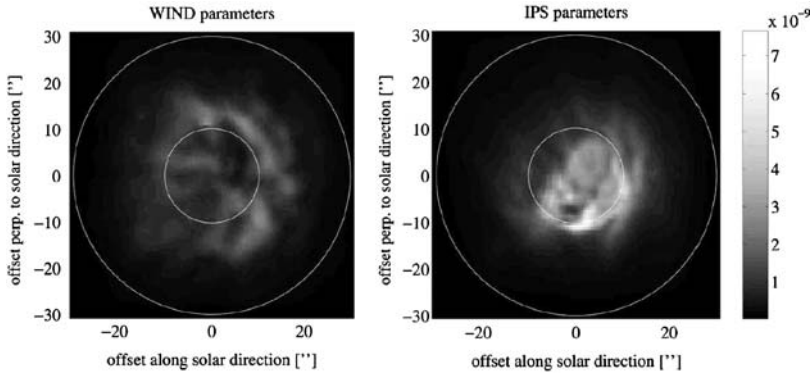

Figure 14. Dependence of the simulated SWCX X-ray images of Mars on the solar wind parameters, for a phase angle of 18.2°. Only the emission of O^{7+} and C^{6+} ions was modeled (from Gunell *et al.*, 2005).

(2004) noted that since crustal magnetizations are asymmetrically distributed, they will also introduce asymmetries in the solar wind flow around the planet and the production of X-rays.

Gunell *et al.* (2005) concluded that due to the sensitive dependence of the properties of the Martian X-ray halo on many parameters, the X-ray emission contains valuable information. However, despite its importance, the statistical quality of the available observational material was extremely poor: all the evidence about an X-ray halo around Mars was based on only $\sim 35 \pm 8$ excess photons and was thus near the sensitivity limit of the Chandra observation (Dennerl, 2002).

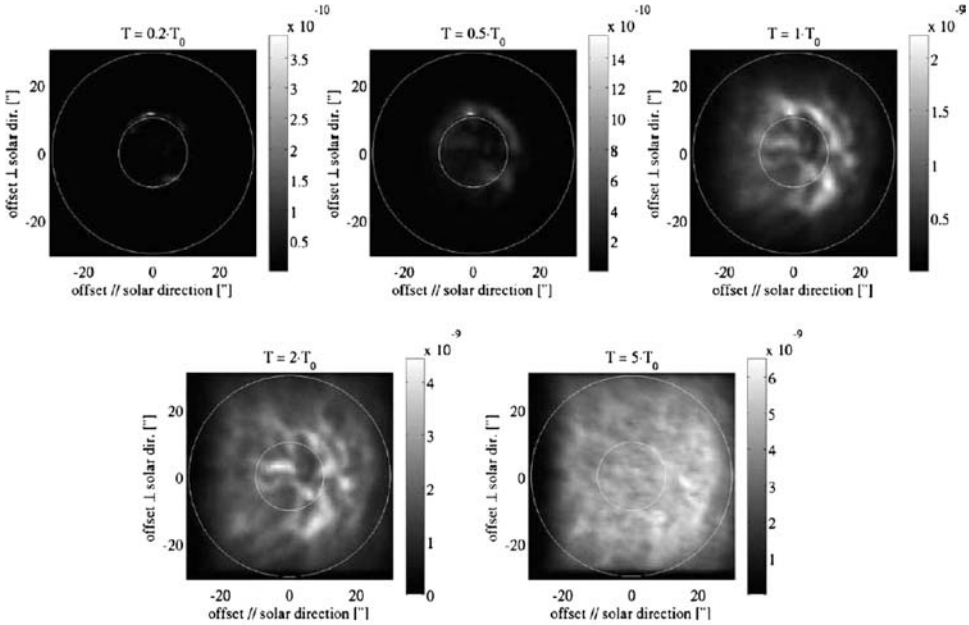

Figure 15. Dependence of the simulated SWCX X-ray images of Mars on the exobase temperature T_0, for a phase angle of 18.2° (cf. Figure 12c). The neutral exosphere was assumed to be spherically symmetric, consisting of atomic and molecular hydrogen and one hot and one thermal population of atomic oxygen, with the following densities ρ and temperatures T_0 at the exobase altitude of 170 km: $\rho(\mathrm{H}) = 3.1 \times 10^{10}$ m^{-3}, $T_0(\mathrm{H}) = 310$ K; $\rho(\mathrm{H_2}) = 4.3 \times 10^{11}$ m^{-3}, $T_0(\mathrm{H_2}) = 370$ K; $\rho(\mathrm{O_{th}}) = 3.3 \times 10^{14}$ m^{-3}, $T_0(\mathrm{O_{th}}) = 380$ K; $\rho(\mathrm{O_{hot}}) = 3.1 \times 10^{10}$ m^{-3}, $T_0(\mathrm{O_{hot}}) = 4600$ K. Only the emission of O^{7+} and C^{6+} ions was modeled (from Gunell *et al.*, 2005).

5. The First XMM-Newton Observation of Mars

This situation improved considerably with the first observation of Mars with the satellite XMM-Newton, on November 19–21, 2003 (Dennerl *et al.*, 2006a,b). XMM-Newton, launched on 10 December 1999, carries three aligned and tightly nested Wolter type I telescopes with a total effective area of more than 0.42 m^2 between 0.1 and 2.0 keV (Jansen *et al.*, 2001), providing the highest throughput currently flying. The X-rays are analysed with three instruments for direct imaging and spectroscopy (EPIC MOS 1, MOS 2, and PN: Turner *et al.*, 2001; Strüder *et al.*, 2001) and with two essentially identical Reflection Grating Spectrometers (RGS 1 and RGS 2), providing an energy resolution $E/\Delta E$ between 100 and and 600 in the energy range 0.33–2.1 keV (den Herder *et al.*, 2001). The main difference to Chandra is that all five X-ray instruments are operating simultaneously, providing higher sensitivity and higher spectral resolution at the expense of reduced spatial resolution and more stringent pointing restrictions.

Observations with XMM-Newton are restricted to targets at solar elongations between 70° and 110°. Thus, Mars cannot be observed around opposition, when it

is closest to the Earth. Within the accessible range of solar elongations, values near 110° are most favourable, because Mars is then considerably closer to the Earth than at smaller elongations. XMM-Newton was pointed towards Mars from 2003 Nov 19, 23:47 to Nov 21, 05:05 UT. At that time, Mars had an apparent diameter of 12.2″. Its heliocentric distance was 1.43 AU, its geocentric distance 0.77 AU, and it was observed at a phase angle (Sun-Mars-Earth angle) of 41.2° and at a solar elongation of 108°.

The XMM-Newton observation confirmed the presence of the Martian X-ray halo and made for the first time a detailed analysis of its spectral, spatial, and temporal properties possible. It proved that the source of the X-ray emission is indeed charge exchange between highly charged solar wind ions and exospheric neutrals, providing the first definite detection of SWCX induced X-ray emission from the exosphere of another planet (Dennerl *et al*., 2006a). Furthermore, it unambiguously showed that the X-ray radiation which we observe from the planetary disk is primarily due to scattered solar X-rays (Dennerl *et al*., 2006b). These new findings are described in the next sections.

5.1. Temporal Properties of the X-ray Emission from Mars

The high sensitivity of the EPIC instruments onboard XMM-Newton made it possible to study the temporal properties of the X-ray emission from Mars with a time resolution of ∼10 min. It turned out that the X-ray flux from Mars was quite variable, exhibiting several outbursts with a characteristic time scale of ∼1 hour. The solar X-ray flux was also highly variable during this time, and the major outbursts show up clearly in the X-ray lightcurve observed from the Martian disk. This is direct proof that this flux is predominantly caused by scattered solar X-rays. At Jupiter (Bhardwaj *et al*., 2005a) and Saturn, (Bhardwaj *et al*., 2005b), a similar correlation has been seen between solar X-ray variability and the planetary X-ray flux.

X-rays were also observed from an extended region around Mars, covering several Mars radii. A lightcurve of the outer regions, between $r \sim 10''$ and $r \sim 50''$, led to an exciting discovery: this X-ray flux was also highly variable, but the variability was not correlated with that observed from the inner region. This is expected if the Martian exosphere responds to variations of the solar wind rather than the solar X-ray emission. Also the spectral properties during outbursts of the inner and outer regions were clearly different from each other, providing additional support to the idea that the X-rays from Mars are a superposition of two different components (Dennerl *et al*., 2006a).

5.2. High Resolution X-ray Spectra of Mars

Although Mars is a very faint X-ray source, the sensitivity of the RGS instruments onboard XMM-Newton was sufficient for performing, for the first time ever, high

TABLE I

Emission lines in the XMM-Newton/RGS Mars spectra (from Dennerl *et al.*, 2006a)

Line ID				Line origin	
#	Abbr	Wavelength [Å]	Energy [eV]	Ion	Transition
1	Ne72	14.21	872.5	Ne^{7+}	$2p \rightarrow 1s$
2	O74	15.18	817.0	O^{7+}	$4p \rightarrow 1s$
3	O65	17.40	712.5	O^{6+}	$5p \rightarrow 1s$
4	O72	18.97	653.6	O^{7+}	$2p \rightarrow 1s$
5	N63	20.91	593.0	N^{6+}	$3p \rightarrow 1s$
6	O6r	21.60	574.0	O^{6+}	$2\,^1P_1 \rightarrow 1\,^1S_0$
7	O6i	21.81	568.5	O^{6+}	$2\,^3P_1 \rightarrow 1\,^1S_0$
8	O6f	22.11	560.9	O^{6+}	$2\,^3S_1 \rightarrow 1\,^1S_0$
9	CO2a	23.50	527.7	CO_2	$1\pi_g \rightarrow 1s$
10	CO2b	23.68	523.5	CO_2	$3\sigma_u \rightarrow 1s$
11	N62	24.78	500.3	N^{6+}	$2p \rightarrow 1s$
12	C55	26.36	470.4	C^{5+}	$5p \rightarrow 1s$
13	C54	26.99	459.4	C^{5+}	$4p \rightarrow 1s$
14	C53	28.47	435.6	C^{5+}	$3p \rightarrow 1s$
15	N22	31.51	393.5	N_2	$2p \rightarrow 1s$
16	C45	32.75	378.5	C^{4+}	$5p \rightarrow 1s$
17	C52	33.74	367.6	C^{5+}	$2p \rightarrow 1s$

resolution X-ray spectroscopy of the Martian atmosphere and exosphere (Dennerl *et al.*, 2006a). Figure 16a reveals that the emission of the Martian X-ray halo (at cross dispersion distances $15'' < |y| < 50''$) consists of many emission lines of similar flux. With the exception of lines #9 and #10, all these lines appear where emission is expected from the de-excitation of highly charged ions (Table I). The lines #9 and #10 are caused by fluorescence of CO_2. They appear in the halo spectrum only because of instrumental effects. However, these lines dominate the RGS spectra from regions close to Mars (at cross dispersion distances $|y| \leq 10''$ from its center; Figure 16b), where the N_2 fluorescence line (#15) is also indicated. These two high resolution spectra clearly show that the X-rays from Mars are composed of two completely different components.

In terms of spectral resolution, Figure 16a shows perhaps the best charge exchange spectrum ever obtained. The high spectral resolution is demonstrated in Figure 17a, which zooms to a small section covering only 3Å (70 eV). All the emission in this spectral region originates from inner shell electron transitions in oxygen, either six-fold ionized or neutral (embedded in CO_2). This spectrum was compiled for cross dispersion distances $|y| \leq 50''$ and includes also emission from Mars itself. It is dominated by CO_2 fluorescent emission,

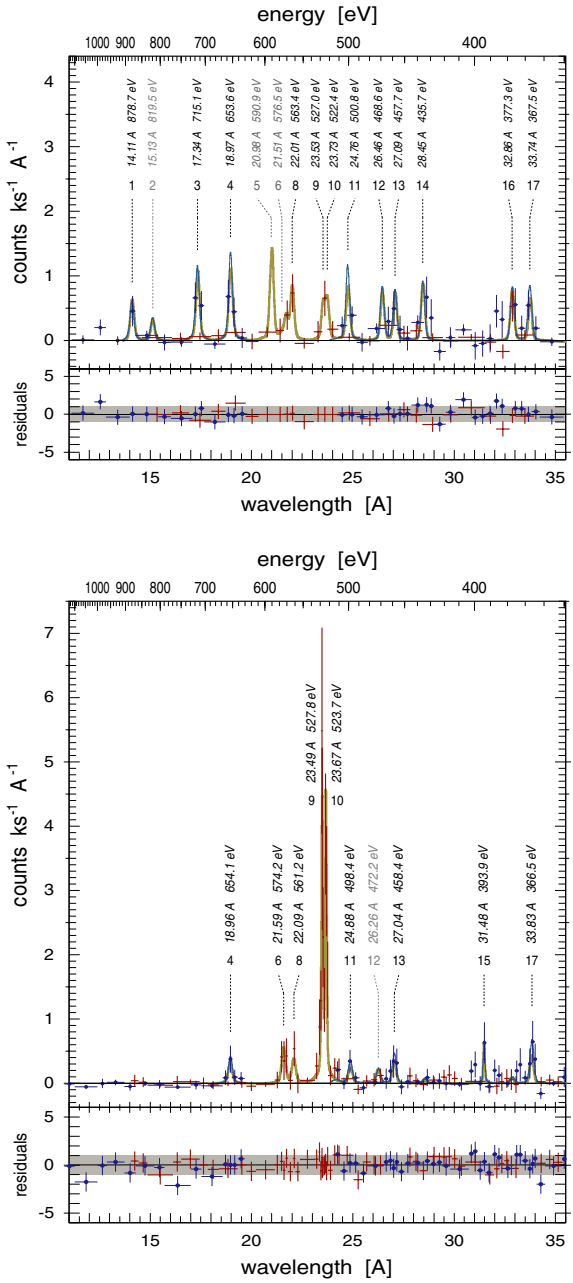

Figure 16. XMM-Newton/RGS spectra of Mars and its halo, accumulated at cross dispersion distances (a) $15'' < |y| < 50''$ and (b) $|y| \leq 10''$ from the center of Mars. Smooth curves show the corresponding folded model spectra, with a thick line for RGS 1 and a thin one for RGS 2. The positions resulting from the fit (in Å and eV) are written above each line, together with a running number, for easier reference (cf. Table I). A zoomed version of the central region around 23 Å/540 eV is shown in Figure 17a (from Dennerl *et al.*, 2006a).

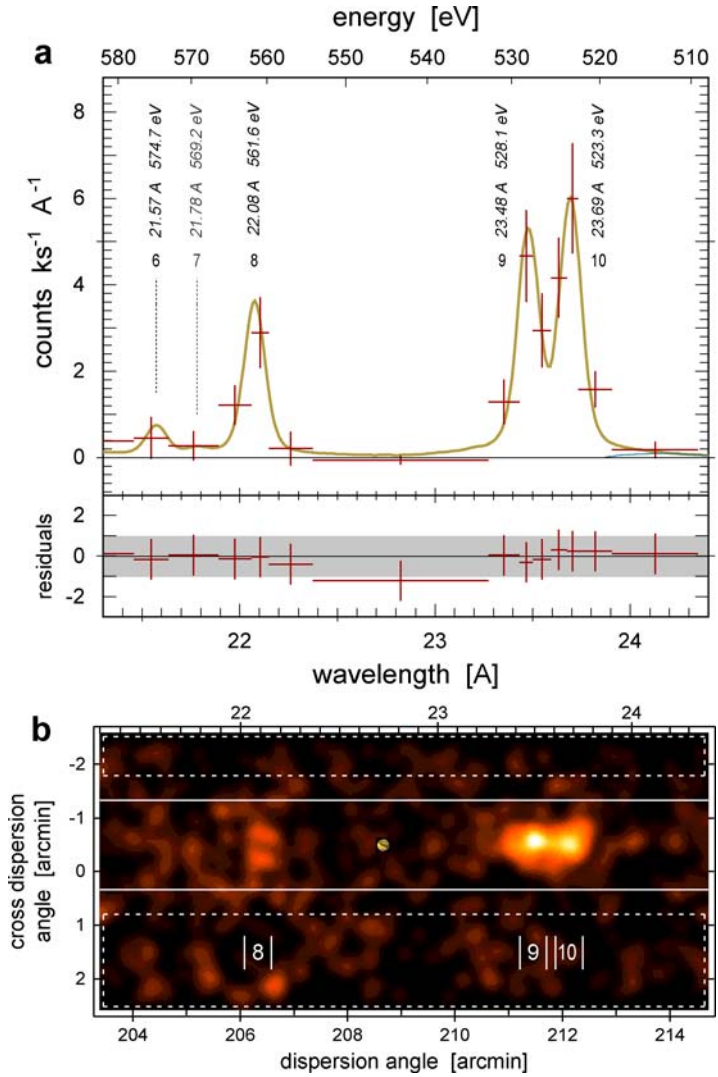

Figure 17. (a) XMM-Newton/RGS 1 spectrum of Mars and its halo at cross dispersion distances $|y| \leq 50''$ from the center of Mars, showing the region around the CO_2 doublet and the O^{6+} multiplet. (b) Dispersed image in the same wavelength/energy scale as in (a). This image was binned into $2'' \times 2''$ pixels and smoothed with a Gaussian function with $\sigma = 8'' \times 8''$. It contains the full FOV of RGS along the cross dispersion direction. The inner rectangle shows the extraction region for the $|y| \leq 50''$ spectra in (a); the background was taken from the two dashed bands above and below. An optical image (taken by the author with a 4" Newtonian telescope) is inserted at the center to illustrate the angular size of Mars during the observation; the observed X-ray images are blurred by the PSF of the telescope and the smoothing process. Note that due to the high dispersion of RGS, the X-ray image of the Martian halo (8) is completely detached from the fluorescent images (9, 10) (adapted from Dennerl *et al*., 2006a).

which is clearly resolved into two lines (#9 and #10) of similar flux. This is the first astronomical measurement of fine structure in the X-ray fluorescence of CO_2.

The explanation for two peaks instead of one is that in the CO_2 atmosphere of Mars, the oxygen atom is embedded in a molecule, where additional energy states are available for the electrons. The line at 528 eV (#9) is caused by an electron transition from the $1\pi_g$ orbital (which is almost a pure $2p$ orbital around the oxygen atom, and thus similar to the isolated oxygen atom state) into the ground state, while the line at 523 eV (#10) is a superposition of transitions from three orbitals, $4\sigma_g$, $3\sigma_u$, and $1\pi_u$, into the ground state.

Of even higher diagnostic value in Figure 17a is the fine structure seen in the emission from O^{6+} ions (lines #6, #7, #8). These lines are the result of electron transitions between the $n = 2$ shell and the $n = 1$ ground state shell. As O^{6+} contains two electrons, there are two possible states of the ion, depending on the relative spin orientation of the electrons: singlet states (mainly $^1S_0$ and $^1P_1$) and triplet states (mainly $^3S_1$ and $^3P_{0,1,2}$). Because transitions from triplet states to the ground state require spin changes of the electrons, these are slow processes compared to transitions from singlet states.

The line #6 results from fast transitions from a singlet state ($^1P_1$) with a decay rate of $3.3 \cdot 10^{12}$ s^{-1}, while the lines #7 and #8 are caused by slow transitions from triplet states. Particularly interesting is the line #8, because the corresponding transition starts from a metastable state ($^3S_1$) and has a decay rate of only $1.0 \cdot 10^3$ s^{-1}. This state can easily be depopulated by collisions before the transition takes place. The fact that the line #8 is considerably brighter than the lines #6 and #7 excludes thermal or collisional excitation as the origin of the Martian X-ray halo emission. For hot plasmas, the flux ratio $G = (\#7 + \#8)\,/\#6$ of triplet to singlet transitions is usually less than one (e.g. Smith *et al.*, 2001).

However, if the emission lines result from electron capture by multi-charged ions colliding with neutral gas at low density, the situation is completely different. In this case, G is predicted to be in excess of three (Kharchenko *et al.*, 2003). The value of the G ratio for the O^{6+} emission induced by the interaction between the solar wind ions and heliospheric hydrogen gas has been evaluated as 6.7 (Pepino *et al.*, 2004), and for the cometary X-rays as 5.8 (Kharchenko, 2005). These values agree very well with that derived from the Mars RGS spectra: $G \sim 6$ for $|y| \leq 50''$. Thus, the high resolution X-ray spectrum in Figure 17a provides the direct proof that the X-ray emission of the Martian halo is indeed caused by the SWCX process.

5.3. X-ray Images of Mars in Individual Emission Lines

As slitless spectrometers, the RGS produce in each spectral line an image of the observed object. Due to the high dispersion of the RGS and the small spatial extent

of Mars, there is essentially no overlap between the individual images. This makes it possible to study the spatial structure of the X-ray emission in individual spectral lines. As fluorescence occurs in neutral atoms and molecules, while charge exchange involves highly charged ions, the energies/wavelengths of the corresponding emission lines are different. Thus, the contributions of fluorescence and charge exchange can be completely separated by this method.

Figure 17b shows the RGS image which corresponds to the zoomed spectrum in Figure 17a, at the same wavelength scale. To illustrate the spatial extent of Mars at the time of the observation, an optical image was inserted at the center. The spectral images of the CO_2 emission to the right (#9, #10) prove that this radiation originates close to the planet, as their brightness distributions peak at the position of Mars. Brightness profiles along the dispersion direction (Figure 18b) show that their extent is consistent with the size of Mars, if the instrumental blur is taken into account, and that there is no significant difference between both components.

The spectral image of the O^{6+}: $^3S_1 \rightarrow {}^1S_0$ transition (#8 in Figure 17b) is completely different from that of the CO_2 emission, exhibiting two distinct blobs along the cross dispersion direction (which is approximately the North-South direction on Mars), with practically no emission in between (Figure 18a). This means that the emission does not originate close to Mars or in an X-ray luminous extended shell around it, but at two well localized regions ~3000 km above both poles. For other emission lines, however, the morphology appears to be different. Figure 19

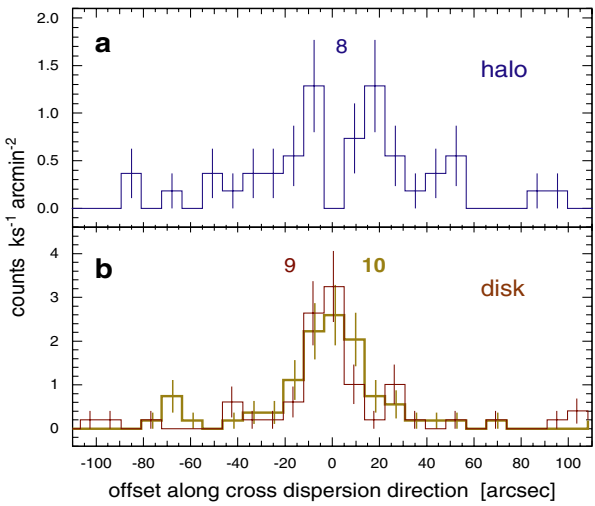

Figure 18. Brightness profiles (with 1σ error bars) along the cross dispersion direction of the Martian exosphere in the light of (a) the $2\,^3S_1 \rightarrow 1\,^1S_0$ transition of O^{6+} (#8) and (b) the CO_2 fluorescence doublet (#9, #10). The extraction geometry is illustrated in Figure 17b. While the CO_2 profiles are very similar, the O^{6+} profile has a quite different shape, characterized by a pronounced dip at the center (from Dennerl *et al.*, 2006a).

presents spectral images for the major emission lines, identified by the abbreviations listed in Table I. These images indicate differences in the spatial structures, not only between fluorescence and charge exchange, but also between different ions and ionization states.

The structure seen in the spectral image of O6f seems to be a specific property of emission from ionized oxygen, as the O72 image (Figure 19a) also shows two distinct blobs along the cross dispersion direction. Compared to O6f (Figure 19b), the O72 emission occurs at larger distances from Mars. There is also some evidence in Figure 19a that the peak of the O72 emission is shifted to the right with respect to Mars. Interpreted as redshift, this would indicate velocities of O^{8+} ions in excess of $\sim$400 km s^{-1} along the line of sight, as the dashed vertical lines in Figure 19a show. Alternatively, this shift may be interpreted as a spatial displacement.

Spectral images can also be obtained for the carbon emission lines C53 and C52 (Figure 19 d,e). Although the quality of these images is limited by statistical noise, they seem to indicate yet another morphology: there is again clear evidence for extended, unisotropic emission, but unlike the blobby O72 and O6f appearance, the C53 and C52 emissions exhibit a more band-like structure without a pronounced intensity dip at the position of Mars. There is also some evidence that at larger distances from Mars the emission is shifted towards the right. For comparison, the morphology of the fluorescent radiation (Figure 19 g–i) is clearly concentrated to the planet. While an interpretation of the fluorescence images is straightforward, an interpretation of the structures in the halo emission is not an easy task, since they depend on many parameters (e.g. Gunell *et al.*, 2005).

Figure 20 is a superposition of RGS images of Mars in seven emission lines between 19 Å and 34 Å (360–660 eV), with ionized oxygen coded in blue, ionized carbon coded in green, and fluorescence coded in yellow. The horizontal axis is approximately the dispersion direction, with wavelength increasing to the right. Along this direction, the angular and linear scale at lower right is valid only if the individual images are purely monochromatic and exhibit no wavelength/energy shift. Alternatively, the velocity scale at upper right illustrates the amount of horizontal displacement which would be caused by the Doppler shift. As the wavelength is not a linear function of dispersion in the RGS, the amount of displacement depends on the wavelength/energy. The two bars enclose the spectral range used, with the upper (shorter) bar referring to the O72 line at 18.97 Å/653.6 eV and the lower bar to the C52 line at 33.74 Å/367.6 eV. A displacement to the right (where wavelength increases) corresponds to a redshift.

Figure 20 reveals that the halo emission originates in an extended region which is elongated mainly along the cross dispersion direction. This alignment, however, is not precise: there are indications for some tilt of the upper and lower wings to the right. As this figure is composed of individual images obtained with a slitless spectrograph, there are generally two possibilities, spectrally or morphologically, for interpreting this tilt:

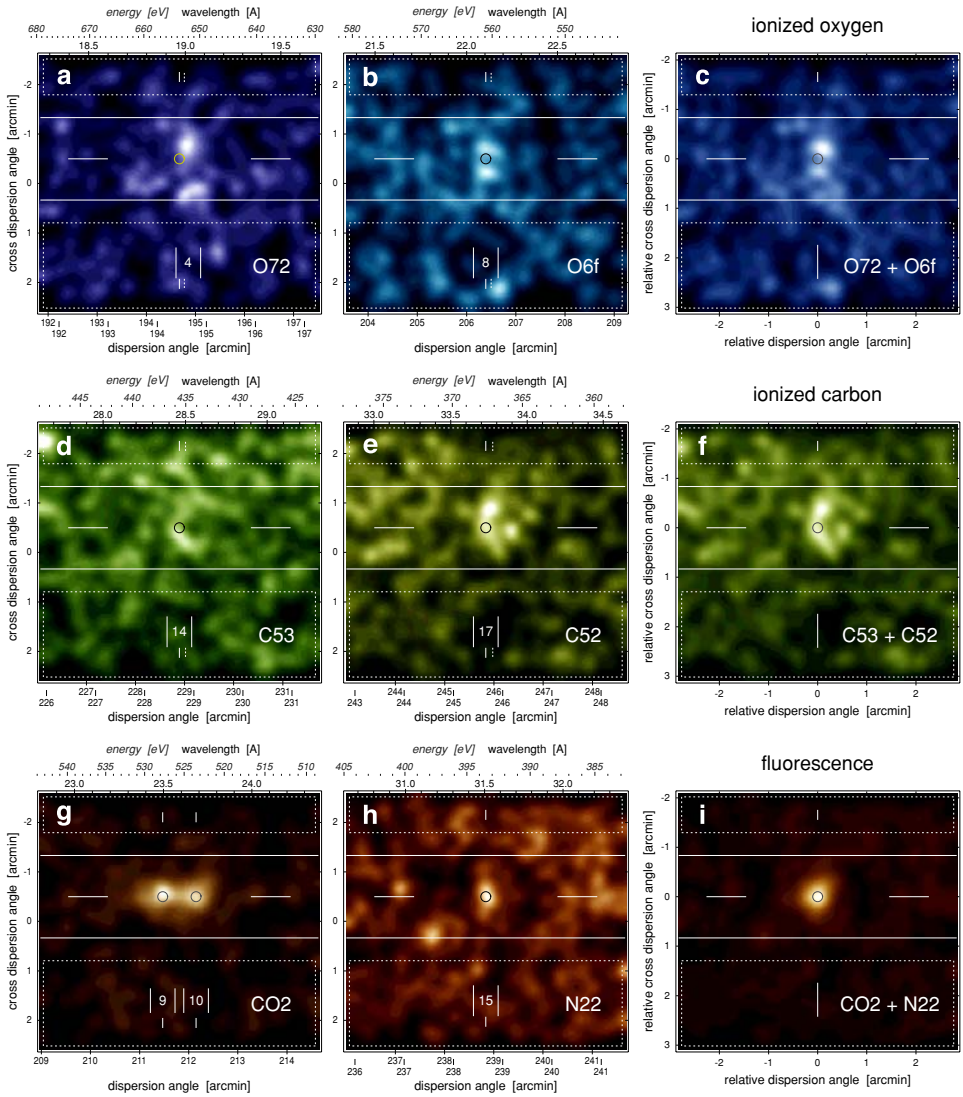

Figure 19. XMM-Newton/RGS images of Mars and its halo in the individual emission lines of ionized oxygen (top row), ionized carbon (middle row), and fluorescence of CO_2 and N_2 molecules (bottom row). The images were corrected for exposure variations, were binned into $2'' \times 2''$ pixels and smoothed with a Gaussian function with $\sigma = 8'' \times 8''$. All are displayed at the same angular scale; the dynamic scale, however, was individually adjusted. The images in the rightmost column are the sum of the images to their left. For the wavelengths/energies of the emission lines, the values in Table I were used. These are indicated by the short vertical lines and the circle in the middle, which illustrates the size and expected position of Mars at these emission lines. Dashed vertical lines in the frames a,b,d,e indicate the apparent shift along the dispersion direction for a redshift of 400 km s^{-1}. The projected direction to the Sun is towards the left (from Dennerl *et al.*, 2006a).

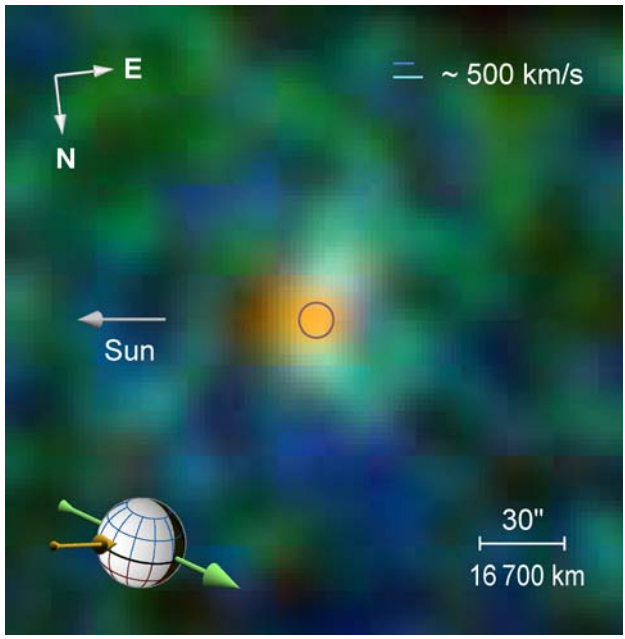

Figure 20. Superposition of the XMM-Newton/RGS images in Figure 19, each centered on the wavelength/energy of an individual emission line, with ionized oxygen coded in blue, ionized carbon coded in green, and fluorescence coded in yellow. The projected direction of the Sun is towards the left (horizontal arrow). The circle indicates the position and size of Mars; further details about the observing geometry are provided by the sphere at lower left: the grid shows areographic coordinates, with blue lines for the southern hemisphere (top) and red lines for the northern hemisphere (bottom). The bright part of the sphere is the sunlit side of Mars. A green arrow indicates its direction of motion, as seen from a stationary point at the position of the Earth. The yellow arrow illustrates the velocity of solar wind particles, emitted radially from the Sun with 400 km s^{-1} with respect to Mars (from Dennerl *et al.*, 2006a).

In the spectral interpretation, this would be evidence for a redshift. The redshift could be explained by the Doppler effect, as the excited solar wind ions are moving away from us. We should expect to observe a Doppler redshift of $\delta\lambda/\lambda \sim (v_i/c)\cos(\varphi)$ where $v_i \sim 400$–800 km s^{-1} is the velocity of the solar wind ions and $\varphi = 41.2^\circ$ is the phase angle of Mars during the XMM-Newton observation. The Doppler shift of the 15–35 Å emission lines may reach the values of 0.015–0.035 Å for the slow solar wind and 0.03–0.07 Å for the fast solar wind. The fact that the observed redshifts decrease with decreasing distance from Mars (along the cross dispersion direction) would be evidence for the fact that the ion velocity decreases towards Mars. i.e., with increasing density of the Martian exosphere. This would be in agreement with model calculations of the solar wind interaction with Mars (e.g. Ma *et al.*, 2004). Part of the deceleration would be a direct consequence of momentum exchange as a by-product of the charge exchange interactions with atoms in the Martian exosphere.

In the morphological interpretation, we see an emission region which is most prominent above the poles, but somewhat tilted away from the Sun. This general appearance may be a consequence of the phase angle at which Mars was observed: if the X-ray emission originates preferentially at the sunward side of the Martian halo, then we should see a crescent-like structure when observing it at a phase angle of 41.2°. This was the result of numerical simulations by Holmström *et al.* (2001), which predicted a crescent-like structure (Figure 13b) that resembles (on a smaller scale) the observed emission in ionized carbon (Figure 19f). The fact that (i) the emission of ionized carbon extends far above the poles and that (ii) the emission of ionized oxygen is observed to occur almost exclusively above the poles could be understood as evidence for an asymmetric density structure in the Martian exosphere, which would be much denser above the poles and towards the night side than towards the Sun.

5.4. Luminosity of the Disk and the Halo

The observed fluxes in the individual emission lines can be converted into luminosities if the angular distribution of the emitted photons is known. For the halo, isotropic emission can be assumed, because the exosphere of Mars is optically thin to X-ray photons, and a halo luminosity $L_x(h) = 12.8 \pm 1.4$ MW is obtained in the spectral band 14–34 Å or 365–880 eV.

For the fluorescence radiation, the situation is different, because the atmosphere of Mars (and the planet itself) is optically thick to soft X-rays. In this case, the luminosity can be computed by spherically integrating the flux as a function of the phase angle (which can be obtained by modeling the individual scattering and absorption processes, as described in Dennerl *et al.*, 2002) over the phase angle (cf. Figure 9). This results in a disk luminosity $L_x(d) = 3.4 \pm 0.4$ MW for fluorescence of oxygen and nitrogen.

It is well possible that the disk spectrum contains also some contribution from elastic scattering of solar X-rays, in addition to fluorescence. This contribution, however, should be small, because no significant unambiguous evidence for elastic scattering is seen in the RGS spectrum. Therefore, the calculation of the disk luminosity was restricted to the oxygen and nitrogen fluorescence lines in the RGS bandpass.

This disk luminosity is significantly higher than the 1.4 ± 0.2 MW derived from the previous Chandra observation (Dennerl, 2002) for oxygen and nitrogen (the carbon fluorescence is just outside the RGS spectral band). An obvious explanation is found in Figure 3: although the XMM-Newton observation took place during the declining part of the solar cycle, this observation happened to fall into a period of extreme solar activity, where the mean solar 1–8 Å flux was almost one order of magnitude higher than during the Chandra observation.

The observed luminosity of the X-ray halo is even more than one order of magnitude higher than in the previous Chandra observation of Mars, which yielded 0.5 ± 0.2 MW in the energy range 0.5–1.2 keV (Dennerl, 2002). This lower value was in good agreement with theoretical predictions (Krasnopolsky, 2000; Holmström *et al*., 2001; Krasnopolsky and Gladstone, 2005).

One reason for the much higher halo luminosity during the XMM-Newton observation is the fact that a considerable flux was observed at large distances from Mars: the Chandra flux was derived from within 3 Mars radii around its center, or $r = 30''$ at the time of the Chandra observation. Outside this radius, no significant excess of surface brightness relative to the Chandra background level was detectable. Applied to the XMM-Newton observation, this radius would correspond to only $18''$, due to the larger geocentric distance of Mars. Thus, the XMM-Newton 'halo region', which was defined here by cross dispersion distances $15'' < |y| \leq 50''$ (e.g. Figure 16a), would have been almost completely outside the Chandra halo region, and this region was found to contain most of the observed flux (cf. Figure 20): the X-ray luminosity in this region alone was 10.0 ± 1.2 MW.

Another reason for the high X-ray luminosity of the halo was the extreme solar activity in October–November 2003: over two solar rotations, ∼80 fast coronal mass ejections (CMEs) were observed together with X-class flares, solar energetic particle events, and interplanetary shocks (Gopalswamy *et al*., 2005). On November 18, a prolonged optical flare occurred, accompanied by two X-ray bursts at 07:52 and 08:31 UT and a CME with multiple components, starting with a comparatively weak ejection, but then followed by a much brighter, faster, and larger-scale partial-halo CME after ∼08:40 UT and a third large CME after 09:26 UT (Chertok and Grechnev, 2005). It is very likely that this sequence of CMEs produced a highly disturbed solar wind environment at Mars during the XMM-Newton observation, which took place 1.63–2.85 days after the second CME. The XMM-Newton EPIC data (Dennerl *et al*., 2006b) exhibit significant variability in the X-ray flux of the Martian halo, including several outbursts by a factor of ∼4 with a duration of about one hour each. Unfortunately, Mars Express had not arrived yet at Mars in November 2003, so that no simultaneous in-situ plasma measurements exist.

6. Summary and Conclusions

X-rays from Mars consist of two different components: (i) solar X-rays scattered in the upper Martian atmosphere, and (ii) emission from highly charged heavy solar wind ions in excited states, resulting from charge exchange interactions with neutrals in the Martian exosphere. For both components, the pioneering observations with Chandra and XMM-Newton have shown how X-ray observations will provide novel methods for studying this planet: high resolution X-ray images of Mars in the fluorescence lines of C, N, O will make it possible to investigate the atmospheric

layers above ∼80 km, which are difficult to study otherwise, and their response to solar activity, while X-ray images of Mars in the lines of excited ions will enhance our knowledge about the Martian exosphere and its interaction with the solar wind.

It is remarkable that XMM-Newton has the capability to trace the exospheric X-ray emission, with high spectral resolution, out to ∼8 Mars radii (∼27 000 km), proceeding into exospheric regions far beyond those that have been observationally explored to date. This is particularly interesting because the X-ray emission results directly from charge exchange interactions between atmospheric constituents and solar wind ions, a process which is considered as an important nonthermal escape mechanism and which may be responsible for a significant loss of the Martian atmosphere. Although this escape process is mainly due to charge exchange with solar wind protons, which are ∼1000 times more abundant than heavy ions and which do not produce X-rays, the X-ray observations by Chandra and XMM-Newton provide a useful tracer of this process. Despite this importance, our observational knowledge of the Martian exosphere is still poor. Thus, X-ray observations, providing a novel method for studying exospheric processes on a global scale, may lead to a better understanding of the present state of the Martian atmosphere and its evolution. They open up a completely new possibility of remote, global, imaging of planetary exospheres, and their spatial and temporal variability.

In addition to its importance to planetary studies, the possibility to obtain from X-ray observations of Mars not only charge exchange spectra with unprecedented spectral resolution, but to get at the same time also images of the morphological structures originating from specific electron transitions in individual ions, is likely to contribute to an improved understanding of the physics of charge exchange, which is of general importance to X-ray plasma diagnostics, both in the laboratory and in outer space.

Acknowledgements

The author would like to thank the anonymous referees for their help in improving the quality of the manuscript.

References

Bhardwaj, A., Branduardi-Raymont, G., Elsner, R. F., Gladstone, G. R., Ramsay, G., Rodriguez, P., *et al.*: 2005a, *Geophys. Res. Lett.* **32**, 3.

Bhardwaj, A., Elsner, R. F., Waite, J. H. J., Gladstone, G. R., Cravens, T. E., and Ford, P. G.: 2005b, *ApJ* **624**, L121.

Chertok, I. M., and Grechnev, V. V.: 2005, *Astronomy Reports* **49**, 155.

Cravens, T. E.: 1997, *Geophys. Res. Lett.* **24**, 105.

Cravens, T. E.: 2000, *Adv. Space Res.* **26**(10), 1443.

Cravens, T. E., and Maurellis, A. N.: 2001, *Geophys. Res. Lett.* **28**(15), 3043.

den Herder, J. W., Brinkman, A. C., Kahn, S. M., Branduardi-Raymont, G., Thomsen, K., Aarts, H., *et al.*: 2001, *A&A* **365**, L7.

Dennerl, K.: 2002, *A&A* **394**, 1119.
Dennerl, K., Burwitz, V., Englhauser, J., Lisse, C., and Wolk, S.: 2002, *A&A* **386**, 319.
Dennerl, K., Englhauser, J., and Trümper, J.: 1997, *Science* **277**, 1625.
Dennerl, K., Lisse, C. M., Bhardwaj, A., Burwitz, V., Englhauser, J., Gunell, H., *et al.*: 2006a, *A&A* **451**, 709.
Dennerl, K., Lisse, C. M., Bhardwaj, A., Burwitz, V., Englhauser, J., Gunell, H., *et al.*: 2006b, *A&A* in preparation.
Gopalswamy, N., Yashiro, S., Liu, Y., Michalek, G., Vourlidas, A., Kaiser, M. L., *et al.*: 2005, *J. Geophys. Res.* **110**, A09S15.
Grader, R. J., Hill, R. W., and Seward, F. D.: 1968, *J. Geophys. Res.* **73**, 7149 .
Gunell, H., Holmström, M., Kallio, E., Janhunen, P., and Dennerl, K.: 2004, *Geophys. Res. Lett.* **31**, 22801.
Gunell, H., Holmström, M., Kallio, E., Janhunen, P., and Dennerl, K.: 2005, *Adv. Space Res.* **36**, 2057.
Holmström, M., Barabash, S., and Kallio, E.: 2001, *Geophys. Res. Lett.* **28**(7), 1287.
Holmström, M., and Kallio, E.: 2004, *Adv. Space Res.* **33**, 187.
Jansen, F., Lumb, D., Altieri, B., Clavel, J., Ehle, M., Erd, C., *et al.*: 2001, *A&A* **365**, L1.
Justus, C. G., Duvall, A. L., and Johnson, D. L.: 2005, *Adv. Space Res.* **35.1**, 4.
Kharchenko, V.: 2005, in R. K. Smith (ed.), *X-ray Diagnostics of Astrophysical Plasmas: Theory, Experiment, and Observation*, Vol. 774, p. 271.
Kharchenko, V., Rigazio, M., Dalgarno, A., and Krasnopolsky, V. A.: 2003, *ApJ* **585**, L73.
Krasnopolsky, V.: 2000, *Icarus* **148**, 597.
Krasnopolsky, V. A., and Gladstone, G. R.: 2005, *Icarus* **176**, 395.
Krause, M. O.: 1979, *J. Phys. Chem. Ref. Data* **8**, 307.
Lisse, C. M., Dennerl, K., Englhauser, J., Harden, M., Marshall, F. E., Mumma, M. J., *et al.*: 1996, *Science* **274**, 205.
Ma, Y., Nagy, A. F., Sokolov, I. V., and Hansen, K. C.: 2004, *J. Geophys. Res.* **109**, A0721.
Metzger, A. E., Gilman, D. A., Luthey, J. L., Hurley, K. C., Schnopper, H. W., Seward, F. D., *et al.*: 1983, *J. Geophys. Res.* **88**, 7731.
Mewe, R., Gronenschild, E. H. B. M., and van den Oord, G. H. J.: 1985, *A&AS* **62**, 197.
Mumma, M. J., Krasnopolsky, V. A., and Abbott, M. J.: 1997, *ApJ* **491**, L125.
Nier, A. O., and McElroy, M. B.: 1977, *J. Geophys. Res.* **82**, 4341.
Owens, A., Parmar, A. N., Oosterbroek, T., Orr, A., Antonelli, L. A., Fiore, F., *et al.*: 1998, *ApJ* **493**, L47.
Pepino, R., Kharchenko, V., Dalgarno, A., and Lallement, R.: 2004, *ApJ* **617**, 1347.
Pfeffermann, E., Briel, U. G., Hippmann, H., Kettenring, G., Metzner, G., Predehl, P., *et al.*: 1986, *Proc. SPIE* **733**, 519.
Reilman, R. F., and Manson, S. T.: 1979, *ApJS* **74**, 815.
Sehnal, L.: 1990a, *Bull. Astron. Inst. Czechosl.* **41**, 115.
Sehnal, L.: 1990b, *Bull. Astron. Inst. Czechosl.* **41**, 108.
Smith, R. K., Brickhouse, N. S., Liedahl, D. A., and Raymond, J. C.: 2001, *ApJ* **556**, L91.
Strüder, L., Briel, U., Dennerl, K., Hartmann, R., Kendziorra, E., Meidinger, N., *et al.*: 2001, *A&A* **365**, L18.
Tobiska, W. K., Woods, T., Eparvier, F., Viereck, R., Floyd, L., Bouwer, D., *et al.*: 2000, *J. Atm. Solar Terr. Phys.* **62**, 1233.
Trümper, J.: 1983, *Adv. Space Res.* **2**(4), 241.
Turner, M. J. L., Abbey, A., Arnaud, M., Balasini, M., Barbera, N., Belsole, E., *et al.,*: 2001, *A&A* **365**, L27.
Wickramasinghe, N. C., and Hoyle, F.: 1996, *Ap&SS* **239**, 121.
Winckler, J. R., Peterson, L., Arnoldy, R., and Hoffman, R.: 1958, *Phys. Rev.* **110**, 1221.
Withers, P.: 2006, *Geophys. Res. Lett.* **33.2**, 10.1029/L02201.